

## Cellular nonlinear networks for strike-point localization at JET

P. Arena, L. Fortuna, M. Bruno, G. Vagliasindi, A. Murari, et al.

Citation: *Rev. Sci. Instrum.* **76**, 113503 (2005); doi: 10.1063/1.2130936

View online: <http://dx.doi.org/10.1063/1.2130936>

View Table of Contents: <http://rsi.aip.org/resource/1/RSINAK/v76/i11>

Published by the [American Institute of Physics](#).

---

### Related Articles

No related articles were found.

---

### Additional information on *Review of Scientific Instruments*

Journal Homepage: [rsi.aip.org](http://rsi.aip.org)

Journal Information: [rsi.aip.org/about/about\\_the\\_journal](http://rsi.aip.org/about/about_the_journal)

Top downloads: [rsi.aip.org/features/most\\_downloaded](http://rsi.aip.org/features/most_downloaded)

Information for Authors: [rsi.aip.org/authors](http://rsi.aip.org/authors)

### ADVERTISEMENT

  
**AIP**Advances

*Submit Now*

**Explore AIP's new  
open-access journal**

- **Article-level metrics  
now available**
- **Join the conversation!  
Rate & comment on articles**

## Cellular nonlinear networks for strike-point localization at JET

P. Arena, L. Fortuna, M. Bruno, and G. Vagliasindi

*Dipartimento di Ingegneria Elettrica, Elettronica e dei Sistemi, Università di Catania, v. le A. Doria 6, I-95125 Catania, Italy*

A. Murari

*Consorzio RFX-Associazione EURATOM ENEA per la Fusione, Corso Stati Uniti 4, I-35127 Padua, Italy*

P. Andrew

*Euratom/UKAEA Fusion Association, Culham Science Centre, Abingdon, Oxon OX14 3DB, United Kingdom*

G. Mazzitelli

*Assoc. Euratom-ENEA sulla Fusione, C.R. Frascati-C.P. 65, I-00044 Frascati (Roma), Italy*

(Received 20 April 2005; accepted 4 October 2005; published online 9 November 2005)

At JET, the potential of fast image processing for real-time purposes is thoroughly investigated. Particular attention is devoted to smart sensors based on system on chip technology. The data of the infrared cameras were processed with a chip implementing a cellular nonlinear network (CNN) structure so as to support and complement the magnetic diagnostics in the real-time localization of the strike-point position in the divertor. The circuit consists of two layers of complementary metal-oxide semiconductor components, the first being the sensor and the second implementing the actual CNN. This innovative hardware has made it possible to determine the position of the maximum thermal load with a time resolution of the order of 30 ms. Good congruency has been found with the measurement from the thermocouples in the divertor, proving the potential of the infrared data in locating the region of the maximum thermal load. The results are also confirmed by JET magnetic codes, both those used for the equilibrium reconstructions and those devoted to the identification of the plasma boundary. © 2005 American Institute of Physics.

[DOI: [10.1063/1.2130936](https://doi.org/10.1063/1.2130936)]

### I. INTRODUCTION AND OVERVIEW

Real-time control is a rapidly expanding subject also in the field of nuclear fusion. In ITER, and even more in the reactor, the number of quantities to be controlled in feedback will be much higher than in present-day machines, given the complexity of the device and the safety issues involved. On the other hand, the operating environment of the next-generation experiments is going to pose severe problems for diagnostics and, as a consequence, for real-time schemes. The high neutron fluence and the steady-state operation are two of the major issues of concern in this perspective. These conditions are expected to affect some of the most fundamental measurements in a Tokamak device, i.e., the magnetic diagnostics, and can therefore potentially create serious difficulties for the most basic control systems. In fact, in present-day machines, magnetic measurements rely on the established technology of pickup coils, the latter having intrinsic problems in coping with long steady-state fields, due to their being based on flux variation. Moreover, high neutron fluence is known to cause several problems to cables, including the generation of common mode currents, which can produce dangerous drifts in the acquired signals. Since the coils have to be located near the plasma in order to avoid the shielding due to the passive conductors, this neutron-induced damage is certainly a serious issue for the next step. Several alternatives are therefore being assessed within the community to integrate the pickup coil measurements with

other diagnostics so as to obtain a more reliable identification of the plasma boundary in ITER. The use of reflectometric data and radiation hard Hall probes are two of the main alternatives presently under investigation. A complementary approach consists of using the visual information derived from infrared and/or visible cameras. This article reports the first results obtained in image processing accomplished with the technology of cellular nonlinear networks (CNNs).

Since the main mission of JET consists in developing integrated scenarios for ITER, many of the efforts in recent years have been devoted to the development of innovative real-time tools.<sup>1,2</sup> Particular attention has been devoted to magnetic measurements, since the requirements of discharges with higher elongation and shape, necessary to improve plasma performance, pose severe demands on equilibrium control. Generally speaking, the real-time reconstruction of the plasma boundary is necessary for plasma control, disruption avoidance, and heat load protection. Above all, the accurate localization of the strike points on the divertor plates is imperative to estimate the power load on the carbon tiles, the recycling properties of the configuration, and, in general, to assess the safety features of the pulse. To this end, the magnetic reconstruction of the separatrix done by the XLOC code<sup>3</sup> has proved to be fairly accurate and quite robust throughout a long period of operation and offline extensive validation. On the other hand, even if long pulses do not seem to constitute a particular threat in the case of JET, it has already been experienced on several occasions that mag-

netic data can suffer from noncontemplated deviations due to eddy currents during fast transient events. In particular, the divertor is lodged in a massive conducting structure under which the diagnostic sensors measuring the magnetic field are positioned: when, for example, the divertor coils command the sweeping of the strike points, the reconstruction of their positions based on these measurements can become particularly critical. Moreover, whereas the strike points are mainly defined by the position of the intersection between the separatrix and the divertor plates, power deposition involves larger areas and depends on the flux expansion of the magnetic-field lines. The fine structure of the thermal load in the divertor is therefore not univocally and simply linked to the position of the separatrix.

In this perspective, visual information from suitable cameras can, in principle, be very useful to verify and complement the magnetic reconstruction of the plasma boundary, providing additional details on the location of the strike points and power deposition. On the other hand, manipulating images in a feedback loop with the necessary time resolution can be problematic since the amount of data to be processed is very high. The approach of CNNs was adopted (see Sec. II) so as to solve this problem, since such an approach is particularly suited for fast computation. The CNNs are an array of simple, identical, locally interconnected nonlinear dynamic circuits called cells.<sup>4</sup> Each cell interacts, via weighted connections, with the cells in the neighborhood of a limited radius. The analog implementation permits a parallel way of processing: in fact, the exchange of information among cells occurs in an extremely short time, represented by the time constant of the single cell. This characteristic of the CNN approach is essential in the case of image processing in real time. The chip implementing the CNN and used to obtain the results reported in this article is the ACE16K, designed by the IMSE-CNM under the European Commission Funded DICTAM project.<sup>5</sup> It consists of two layers of CMOS components. The first is the actual sensor whereas the second comprises the architecture necessary to implement the CNN. This innovative system on chip (SOC) technology was used to process the images of JET infrared cameras (Sec. III), using a particular procedure explicitly developed for this application (see Sec. IV). The positive results obtained in the evaluation of the strike-point position are shown in Sec. V, where a systematic comparison with the estimate of XLOC and the divertor thermocouples is also reported. The remaining issues and the lines of future works are discussed in the final Section.

**II. CELLULAR NEURAL NETWORKS FOR IMAGING APPLICATIONS**

The CNN was introduced by Chua<sup>4,6</sup> in 1988 to be employed in such areas as image processing and pattern recognition. The architecture of the CNN is made up of a basic circuit called a cell, containing linear and nonlinear circuit elements (see Fig. 1).

Each cell in a CNN is connected to its local neighboring cells, so a direct interaction occurs only among adjacent cells. An example of a two-dimensional CNN is shown in Fig. 2.

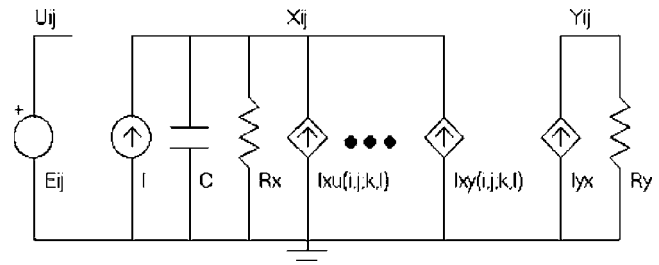


FIG. 1. The classical CNN cell scheme.

The neighborhood of the cell on the *i*th row and *j*th column, denoted by  $C(i, j)$ , has the following definition:

$$N_r(i, j) = \{C(k, l) | \max\{|k - i|, |l - j|\} \leq r, \\ \times 1 \leq k \leq M; \quad 1 \leq l \leq N, \quad (1)$$

where *r* is a positive integer number, which fixes the dimension of the neighborhood.

A CNN is entirely characterized by a set of nonlinear differential equations associated with the cells in the circuit. The mathematical model for the state equation of the single cell, also called full signal range (FSR), as implemented in the CNN universal chip family,<sup>7</sup> is given by the following set of equations:

$$C_x \frac{dx_{ij}(t)}{dt} = -\frac{1}{R_x} g[x_{ij}(t)] + \sum_{C(k,l) \in N_r(i,j)} A(i, j; k, l) y_{kl}(t) \\ + \sum_{C(k,l) \in N_r(i,j)} B(i, j; k, l) u_{kl}(t) + I, \quad (2)$$

$$y_{ij}(t) = x_{ij}(t), \quad (3)$$

where *u*, *x*, and *y* denote the input, state, and output of the cell, respectively;  $R_x$  and  $C_x$  are the values of the linear resistor and linear capacitor that determine the time constant of the circuit;  $A(i, j; k, l)$  and  $B(i, j; k, l)$  are the feedback and control templates, respectively; *I* is the bias term, which is constant for all the CNN cells;  $g(x)$  is the nonlinear function in the state equation (2), depicted in Fig. 3. This last element is the main difference between the classical Chua-Yang CNN model<sup>4</sup> and the FSR model. In Espejo et al.<sup>7</sup> it has been demonstrated that the two mathematical models are equivalent.

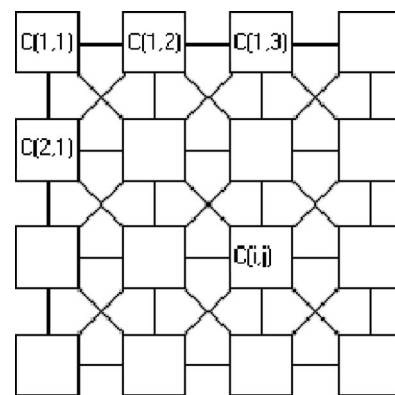


FIG. 2. The CNN scheme.

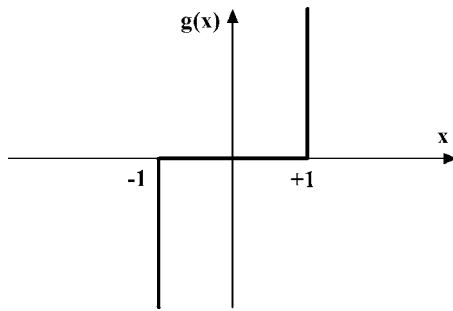


FIG. 3. Nonlinear function in the full signal range CNN model, as implemented in the CNN chip.

As previously reported, one of the main applications of CNNs is image processing.<sup>8,9</sup> In this case, the input image is mapped on the CNN in such a way that each image pixel is associated with the input or initial state of a particular cell. The CNN evolution implies a transformation of the input image into the corresponding output image obtained directly by Eq. (2). In this context, the template operators work like the instructions in a programming code. Even if a direct procedure to derive the template values according to the particular task has not been derived yet, a huge amount of templates and template algorithms is already available in the literature.<sup>10</sup>

The hardware prototype system used in this application is based on two fundamental parts: the CNN Universal Chip prototype, which is a  $128 \times 128$  CNN chip,<sup>11</sup> and the CNN Chip Prototyping and Development System (CCPS) platform designed in Budapest.<sup>12</sup> The chip is a new generation  $128 \times 128$  Focal-Plane Analog Programmable Array Processor (FPAPAP), manufactured in a  $0.35 \mu\text{m}$  standard digital 1P-5M CMOS Technology. It contains close to 4 million transistors, 80% of which work in analog mode, and exhibits a relatively low power consumption ( $<4 \text{ W}$ , i.e., less than  $1 \mu\text{W}$  per transistor). Computing versus power peak values are in the order of  $1\ 82.5 \text{ GOPS/W}$ , while maintained VGA ( $640 \times 480$ ) processing throughputs of 100 frames/s are possible with about 10–20 basic image processing tasks on each frame. The architecture of the system is sketched in Fig. 4.

ACE16K can be described basically as an array of  $128 \times 128$  identical, locally interacting, analog processing units designed for high-speed image processing tasks requiring moderate accuracy (around 8 bits). The system contains a set of on-chip peripheral circuitries that, on the one hand, allow a completely digital interface with the host, and on the other provide high algorithmic capability by means of conventional programming memories where the algorithms are stored.

Although ACE16K is essentially an analog processor (computation is carried out in the analog domain), it can be operated in a fully digital environment. For this purpose, the prototype incorporates a bank of digital-to-analog (for input) and analog-to-digital (for output) converters at the images I/O port. ACE16K is conceived for use in two alternative ways. First, in applications where the images to be processed are directly acquired by the optical input module of the chip, and secondly, as a conventional image coprocessor working in parallel with a digital hosting system that provides and

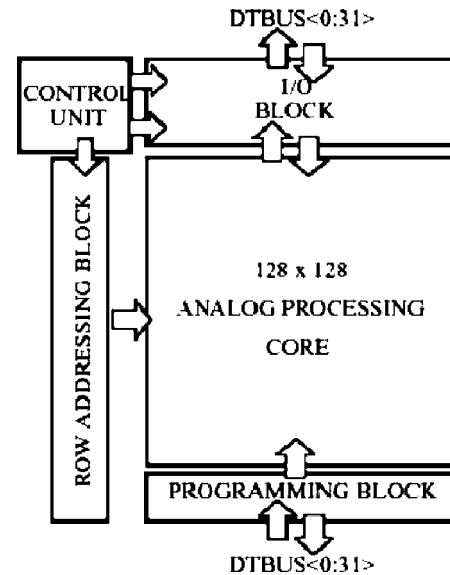


FIG. 4. Block diagram of the ACE16K chip.

receives the images in electrical form. The second mode of operation is the one adopted to obtain the results presented in this article.

The chip can be divided into five functional blocks. The first one is the analog processing core, which comprises the inner array of  $128 \times 128$  identical cells, a ring of border cells used to establish spatial boundary conditions for image processing, and several buffers driving analog and digital signals to the cell array. The second block is the programming block, which contains two  $64 \times 32$  SRAM digital memories used to store the algorithms to be executed by the chip, six  $32 \times 32$  SRAM digital memories used to store, in 8-bit format, different sets of the analog coefficients controlling the cell-to-cell interactions, some global bias signals, and some references used by the optical input module (precharging values, etc.). The programming memory also contains all the circuitry needed for external accesses to these memory blocks, and for the transmission of the programmed values to the analog processing core. This includes digital buffers for digital instructions, and digital-to-analog converters and analog buffers for weights (cell-to-cell interactions) and references. The remaining blocks are dedicated to image I/O tasks. The global I/O control unit generates the signals required for I/O image accesses. This includes row and column addressing signals (automatically generated in a sequential way), and control of the digital-to-analog and analog-to-digital I/O converters bank.

The chip uses a 32-bit bidirectional data bus for external communication and several address buses for the different blocks within the programming memory. The external interface follows very simple handshaking protocols. Table I summarizes the main characteristics of the prototype.

### III. JET DIVERTOR AND THE DIAGNOSTICS FOR THE DETERMINATION OF THE STRIKE POINTS

In Tokamak plasmas, the divertor is the region of the vacuum vessel explicitly designed to handle power losses. In JET history, several topological solutions have been tested as

TABLE I. ACE16K technical characteristics.

ACE16K professional board	
Operation	Frame rate timing
Grayscale image download ( $128 \times 128$ )	2688 frame/s; 372 $\mu$ s
Grayscale image readback ( $128 \times 128$ )	3536 frame/s; 283 $\mu$ s
Array operation ( $128 \times 128$ )	9 $\mu$ s + N*100 ns
Logical operation ( $128 \times 128$ )	3.8 $\mu$ s

far as the divertor is concerned. The one used for the discharges, whose results are described in this article, is shown schematically in Fig. 5. The typical X-point plasma configuration is also shown: it is characterized by the existence of a separatrix and a scrape-off layer. The first one is the last closed flux surface that separates the closed magnetic-field lines from the open ones that intersect the vacuum vessel, while the scrape-off layer is the region of the plasma where the magnetic-field lines intersect wall elements, in this case the divertor. The plasma power losses are deposited along this region. The intersection of the separatrix with the divertor target plate represents a strike point.

In JET, the position of the strike points is mainly derived from magnetic measurements. They consist of various loop and pickup coils located around the vacuum vessel. These measurements, performed at some distance from the plasma, can be extrapolated across the current-free region to identify the last closed flux surface. The code used at JET to determine the plasma shape and therefore also the position of the strike points is XLOC. The main output of XLOC consists of the definition of the last closed flux surface, also called the separatrix.

In the JET divertor, various thermocouples are also located in the divertor tiles, covering the whole region where the magnetic-field lines can intersect material surfaces. The region of maximum thermal load, which can be considered as the position of the strike points, can be identified thanks to thermocouple signals.

Infrared imaging is another very useful diagnostic to derive information about the power deposition in the JET divertor. Nowadays, two cameras are available at JET. They measure the infrared radiation in the interval  $3\text{--}5\ \mu\text{m}$  with a resolution of  $128 \times 128$  pixels. They have, respectively, a vertical and a periscope view of the divertor region. The latter of the two is the one taken into consideration during this study. The periscope camera has a split view in order to capture in a single frame of data both the inner and the outer

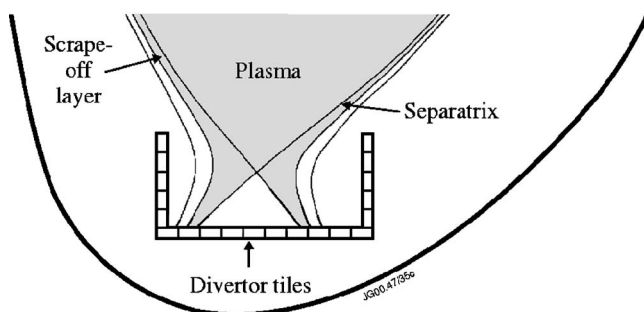


FIG. 5. Schematic outline of JET divertor topology.

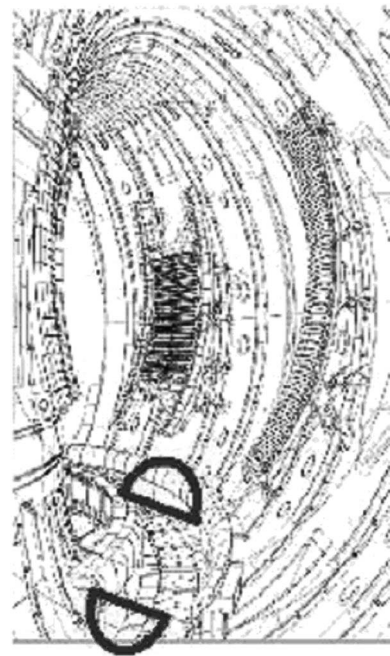


FIG. 6. IR views of the divertor.

part of the divertor. As far as real-time control is concerned, these two views can be considered representative of the entire divertor, given the toroidal symmetry of the machine. The view of the camera is reported in Fig. 6.

The first analysis of the infrared emission had the aim of determining how the presence of the strike points reflects itself in the visual features of the camera images. In Fig. 7, an image captured by the infrared camera is shown. As already mentioned, the strike points represent the region of maximum thermal load on the divertor region. Therefore, the strike points can be identified as the region of maximum brightness in an infrared image. A first manual analysis of images from JET IR cameras proved that the shape of the strike points consists of two thin bands of high emission in the whole divertor region, oriented in the toroidal direction. These last two visual features obviously depend on the posi-

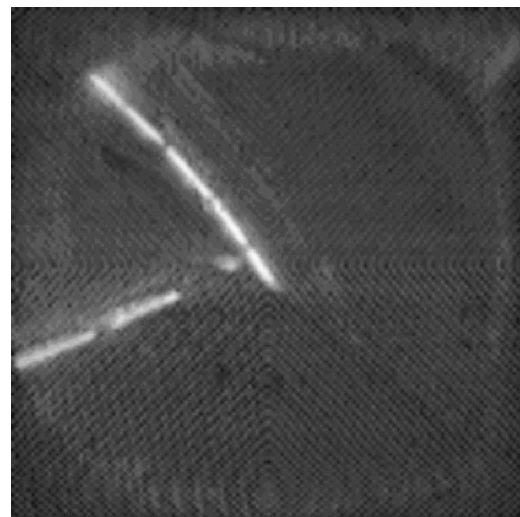


FIG. 7. A typical image from the KL3 infrared camera.

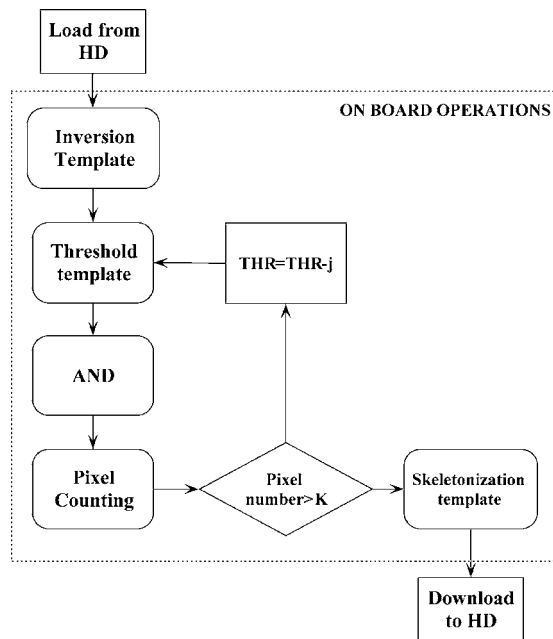


FIG. 8. Flow diagram of the implemented algorithm.

tion and tilt of the camera, but they can be considered invariant in this application, as the camera is installed in a fixed position and orientation.

The second preliminary analysis step was dedicated to camera calibration, which, in the context of three-dimensional (3D) vision, is the process of determining the internal camera geometric and optical characteristics (intrinsic parameters) and the 3D position and orientation of the camera frame relative to a certain world coordinate system (extrinsic parameters). Extrinsic parameters are needed to transform object coordinates into a camera-centered coordinate frame. The pinhole camera model adopted is based on the principle of collinearity, where each point in the object space is projected by a straight line through the projection center into the image plane. The main problem is the perspective projection, which normally is not a shape-preserving transformation. Only lines are mapped as lines on the image plane. Two- and three-dimensional objects with a nonzero projection area are distorted if they are not coplanar with the image plane. The aforementioned problems were solved using dedicated 3D graphic software.

In the CNN algorithms described in the next section, the geometry of the divertor was used as an input together with the coordinates in physical space and the geometrical properties of the cameras. The mapping of the pixels onto the physical space of the divertor is therefore a consolidated input that is used to determine the real position of the strike points once their position in the image acquired by the camera has been determined.

#### IV. THE ALGORITHM FOR THE REAL-TIME IDENTIFICATION OF THE STRIKE POINTS

A specific procedure was developed to derive the position of the strike points from the data of the infrared cameras exploiting the capabilities of CNN technology. A flowchart of the developed algorithm is depicted in Fig. 8.

The algorithm has been applied to a frame extracted from the movie. This frame is the composition of the two images framing, respectively, the inner and the outer side of the divertor region (Figs. 6 and 7). These images should have really different brightness, which varies according to the different temperature the strike points reach in the two regions of the divertor. So it is necessary to perform an independent processing procedure for each one of them.

The first operation, after loading the image from the hard disk, is an *INVERSION* to obtain the negative frames. This is necessary since the CNN-UM works in a grayscale that is inverted with respect to the usual image processing software. Subsequently, a *THRESHOLD* template is applied to the image, to identify the pixels whose value is higher than a predefined level. The result of this first processing phase is a binary image, where the black pixels represent those exceeding a given brightness threshold. In order to perform the independent processing of the two strike points, at this stage an *AND* operation with a mask is executed to select the pixels representing the inner (outer) strike points. To have a number of maxima useful to perform the identification of the strike-point position, the number of pixels in the image is evaluated. If it is less than a given number  $K$ , the threshold value in the *THRESHOLD* template is decreased by a constant value  $j$ , and the cycle is repeated. Otherwise the *LOOP* stops when the  $K$  value is reached. In the algorithm implemented, the  $K$  value is 50 pixels and the threshold constant decrement is set to 10.

At this stage, the images of the strike points consist of a band of black pixels, corresponding to the region of maximum brightness in the divertor legs. Subsequently, a *SKEL-ETONIZATION* template is applied to find the skeleton of the black-and-white bands. Once the skeleton of the inner strike point is obtained, the algorithm is executed once again, this time starting from the inverted image, to extract the outer strike-point position. Finally the results of the algorithm are stored in two picture files in the local hard drive. The various steps of the procedure described above are illustrated graphically in Fig. 9.

The above-mentioned approach can supply the position of both the inner and the outer strike points, including frame loading, within 30 ms. In particular, the onboard operations, i.e., the instructions included in the broken line square in Fig. 8, are executed in a time comprised between 13 and 19 ms, depending on the brightness condition of the starting frame. The loading and downloading of the file from the hard drive takes the remaining 11 ms. This last time can be definitely improved by using better performing hardware to host the Aladdin Platform. This time resolution is already more than acceptable for the vast majority of JET applications. It is indeed necessary to consider that in general the thermal effects, which can affect the tile temperature and change infrared emission, do not change much on shorter time scales. (See Table II.)

#### V. EXPERIMENTAL RESULTS

In order to assess the accuracy of the CNN estimate of the strike-point position, a systematic comparison with the

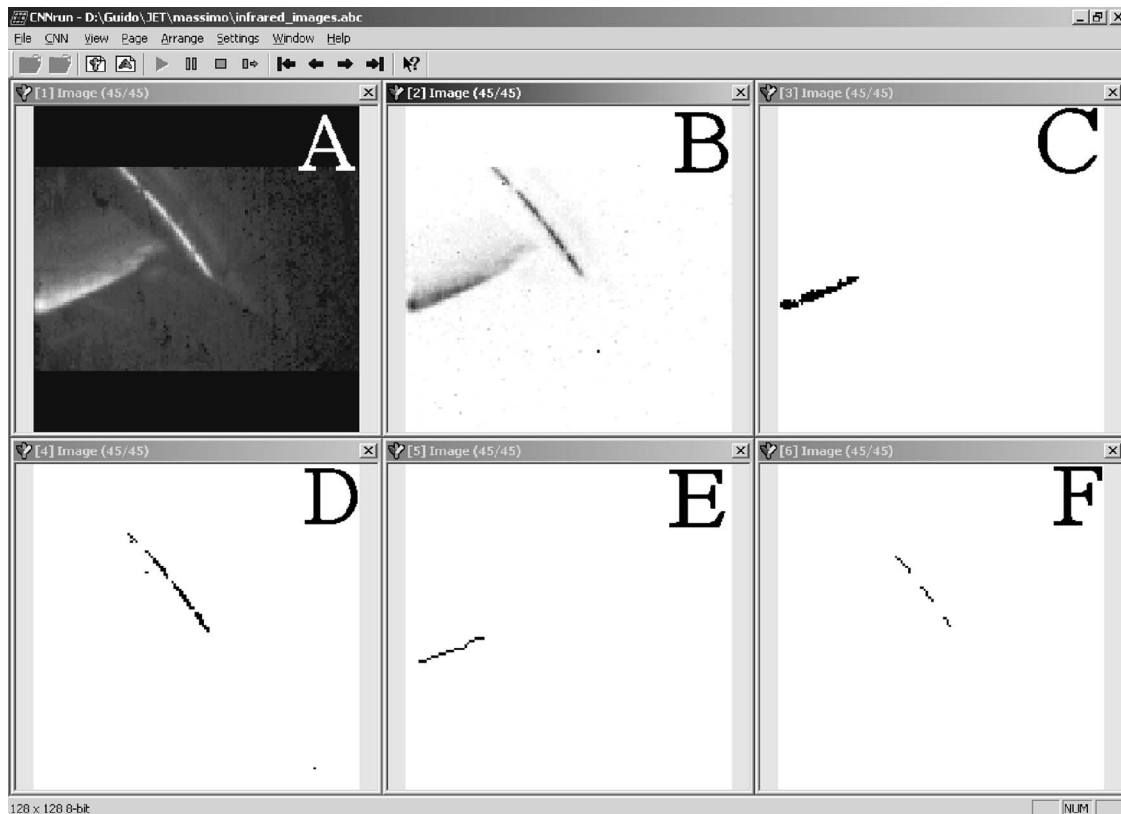


FIG. 9. A CNN run screenshot. Frame *A* is the starting image, frame *B* is the result of the inversion template, then *C* and *D* are the result of the dynamic threshold for the inner and the outer strike leg, respectively, and *E* and *F* are the final images after the skeletonization template.

results of XLOC was undertaken. To this end, the coordinates of the strike points obtained with the CNN were compared with the ones given by XLOC for the intersection of the separatrix with the divertor. As far as this last point is concerned, it is worth mentioning that to detect the intersection of the separatrix calculated with XLOC and the divertor, an approximated shape of the divertor region is used, which is reported in Fig. 10. The lines that represent the approximated divertor are the dashed ones.

The divertor region consists of two parts, the inner and the outer one, as reported in Fig. 10. The intersection of the separatrix with the divertor region always produces four coordinates, two for the inner and two for the outer divertor region, that represent the  $R$  and  $Z$  positions ( $R$  radial,  $Z$  vertical) at which the separatrix crosses the dashed line reported in Fig. 10.

In Figs. 11–14, a comparison between the results obtained with XLOC and those obtained with the CNN image processing for the inner and the outer divertor region is reported. A certain similarity between the two diagnostics can be appreciated, but a clear systematic discrepancy is also

evident in both the  $R$  and  $Z$  position. The discrepancy is to be ascribed to the fact that, due to the flux expansion, usually the maximum power load does not always occur exactly at the position where the separatrix intersects the divertor tiles but it is slightly shifted outward. A much stronger similarity with the magnetic measurements was indeed found when this effect was taken into account. This was achieved considering the intersection with the divertor of the magnetic lines just outside the last closed flux surface. In particular, we used two field lines 5 and 10 mm outside the separatrix (the 5 and 10 mm refer to the position of the field line as calculated at the equatorial plane). In Figs. 11–14, the interceptions calculated for these two lines, obtained by using the EFIT equilibrium code, are reported. It is possible to observe that the CNN calculated values are almost always in the range of the XLOC separatrix and the 10 mm outside flux line, in accordance with the fact that the maximum power load, i.e., what is detected by the CNN approach, is located in a point inside the scrape-off layer.

In order to confirm that the original discrepancy was due to the shift of the point of the maximum power load with respect to the intercept of the separatrix with the divertor tiles, a survey of the thermocouple signals was also performed. In Figs. 15 and 16, the typical evolution in time of the strike points estimated by XLOC, the coordinates obtained by the CNN and the position of maximum load as given by the thermocouples are compared. In JET indeed an array of thermocouples determines the poloidal topology of the tile temperature in the divertor (see Fig. 10). Even though the

TABLE II. Execution time of the algorithm.

Operation	Time (ms)
Load from HD	2 ms
Onboard operations	13–19 ms
Download to HD	9 ms
<b>TOTAL</b>	<b>30 ms</b>

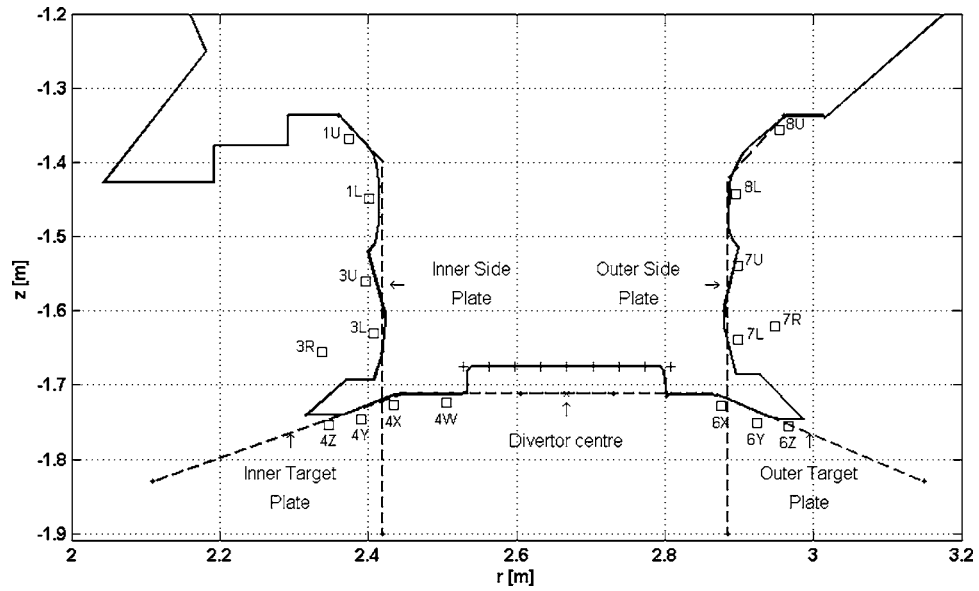


FIG. 10. A detailed view of JET divertor section in the poloidal plane. The blue squares represent the thermocouples located in the tiles.

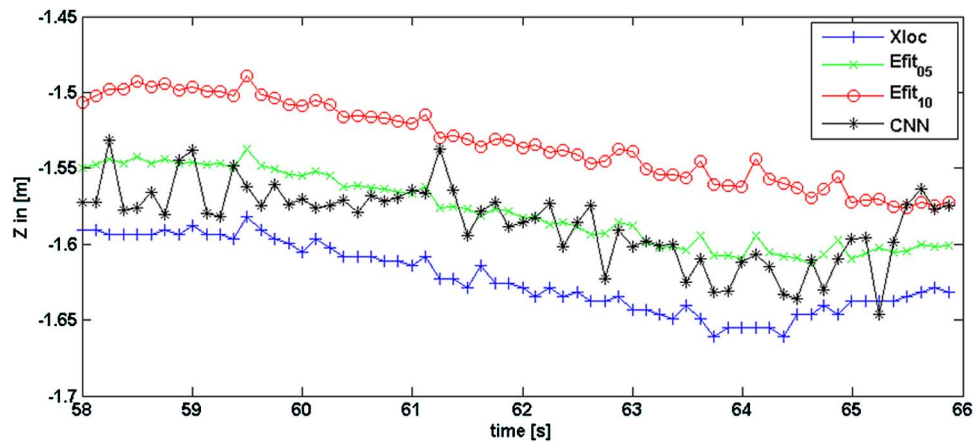


FIG. 11. Comparison of CNN- xLOC separatrix and flux expansion line at 5 and 10 mm for the inner strike point (shot No. 62216).

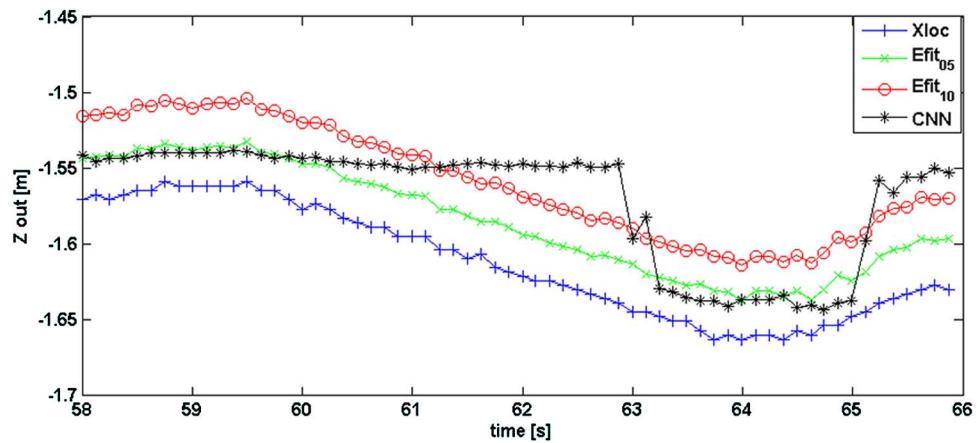


FIG. 12. Comparison of CNN- xLOC separatrix and flux expansion line at 5 and 10 mm for the outer strike (shot No. 62216).

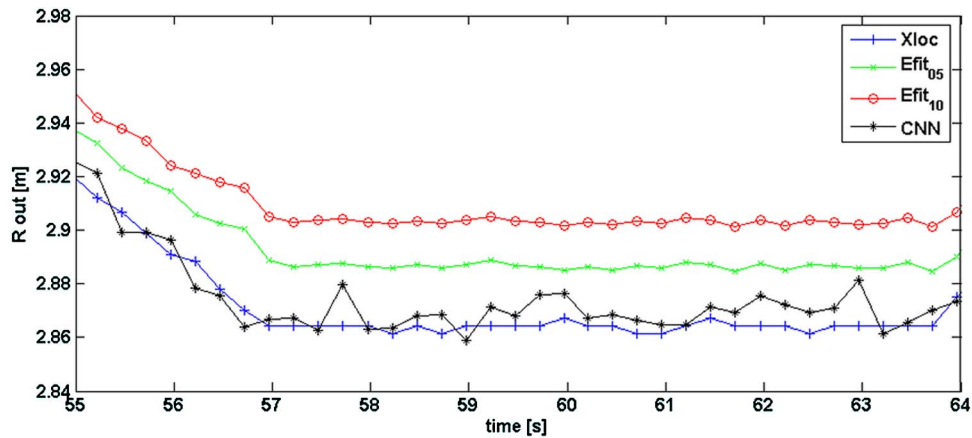


FIG. 13. Comparison of CNN- XLOC separatrix and flux expansion line at 5 and 10 mm for the outer strike (shot No. 59355).

spatial resolution of the array is quite coarse, quite accurate information can be derived on the peak thermal load, when the strike points are close to the position of one of the thermocouples.

As shown in Figs. 15 and 16, the coordinates of the strike points as estimated by the CNN are in accordance with the results of the thermocouples. In fact, in Fig. 15 (bottom) the trend of the thermocouple suggests that the strike point is located in the region of the thermocouples 3U and 3L, as confirmed by the trend of the strike-point coordinates calculated by the CNN. In Fig. 16, the thermocouple trend suggests that the strike point is located first really near the position of 7U and then, after second 63, it moves to 7L. The value calculated using infrared data is in agreement with this trend: during the first phase of the shot evolution, the strike position is located really near the 7U location and then it moves toward the 7L location almost at the same time when the temperature of this thermocouple rises.

To confirm the validity of our approach, a statistical comparison between the CNN estimate and the one derived from the magnetic reconstruction of the boundary was performed. In Fig. 17, the  $x$  axis shows the  $Z$  value calculated with the CNN approach, while the  $y$  axis reports the vertical interception of the flux line 5 mm outside the separatrix calculated via the EFIT software. The congruity between the two results is good: it can be noticed that the absolute error is

included in the range  $[-1 \text{ cm}; +1 \text{ cm}]$  apart from some sporadic points.

## VI. DISCUSSION

As expected, the infrared emission contains a lot of useful information about the position of the strike points, and therefore makes even the study of the fine structure of the power load possible. Moreover, the recent developments of CNN algorithms and the progress in SOC technology make the analysis of visual data much faster, with time scales compatible with the real-time requirements of big tokamaks like JET. As a consequence, the proposed approach becomes quite attractive because it provides information about the maximum power deposition in the divertor but with high spatial and time resolution. This technique, therefore, can in a certain way bridge the performance gap between the magnetic signals and the thermocouples. In any case, the reported results witness that they are highly in accordance with both the XLOC and the thermocouple measurements.

The described approach consists of a smart sensor obtained with CNN mathematical procedures implemented on a single chip. Together with the identification of MARFE at FTU,<sup>13</sup> this is the first use of SOC technology in the fusion community. It is worth pointing out that similar systems, based on CMOS technology and CNN algorithms, could find

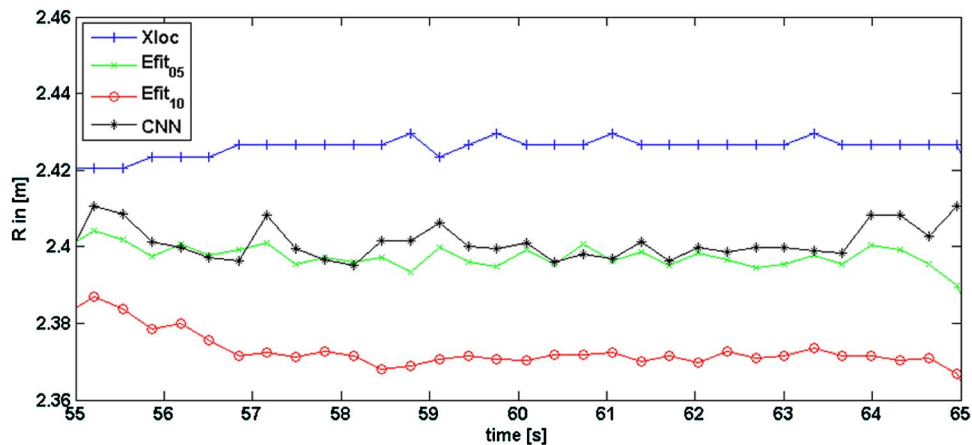


FIG. 14. Comparison of CNN- XLOC separatrix and flux expansion line at 5 and 10 mm for the inner strike (shot No. 61927).

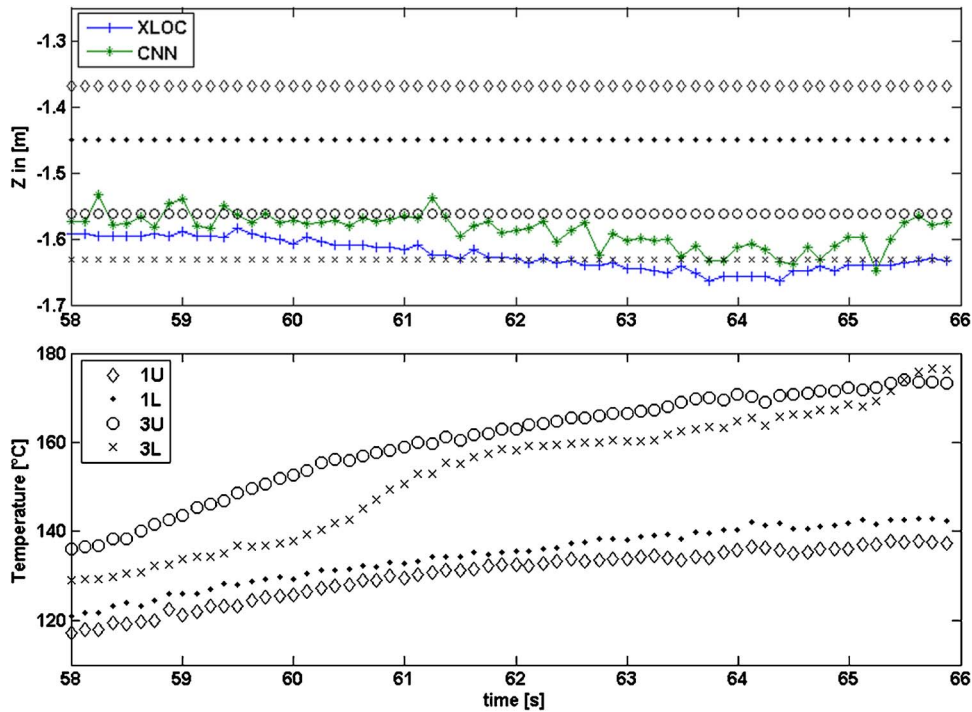


FIG. 15. In the top figure, the time evolution of the CNN and XLOC calculated strike points is shown, together with the position of the corresponding thermocouple for the coordinate Z in the inner side of the divertor. In the bottom figure, the time evolution of the thermocouples temperature is shown (shot No. 62216).

other useful applications in JET, for example in the detection of the hot spots and control of the beam shine-through.

In any case, in order to increase the potential of the presented approach for the identification of the strike points on the route to ITER, some improvements remain necessary. First of all, the CMOS technology should be miniaturized

even further to increase the speed up to about 1 ms time resolution. Moreover, in order to use the chip as a self-contained detector without having to make recourse to infra-red camera signals, the potential to develop a first layer sensitive to IR radiation is being investigated. Also, the alternative to exploit visible radiation should not be com-

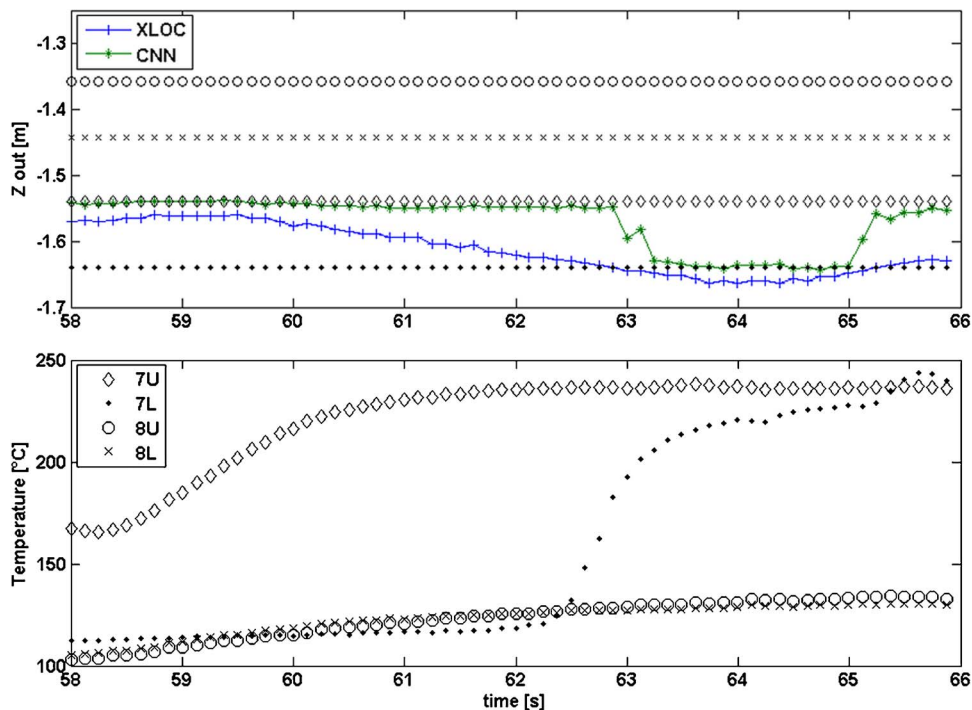


FIG. 16. In the top figure, the time evolution of the CNN and XLOC calculated strike points is shown, together with the position of the corresponding thermocouple for the coordinate Z in the outer side of the divertor. In the bottom figure, the time evolution of the thermocouple temperature is shown (shot No. 62216).

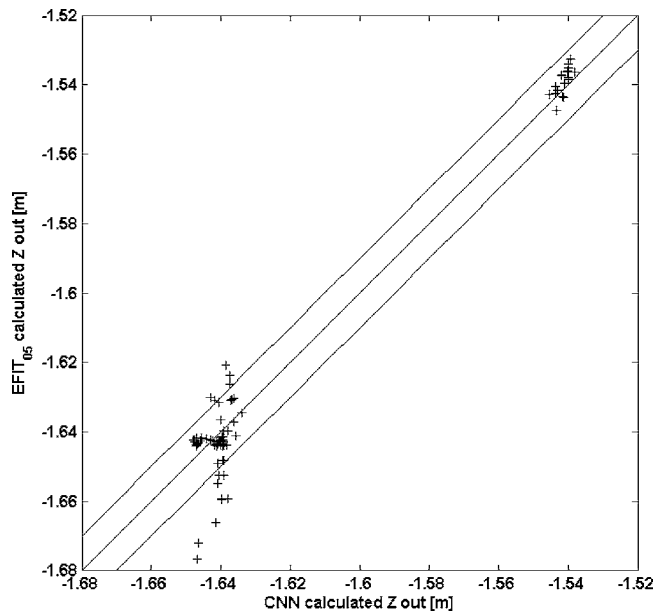


FIG. 17. Comparison of the Z estimate of the outer strike point as derived from the CNN and EFIT<sub>05</sub>.

pletely dismissed *a priori* and further tests are planned in this direction. In the perspective of diagnosing a burning plasma, the radiation hardness of the technology should also be assessed.

## ACKNOWLEDGMENT

The work was partially supported by the Project “Real-time visual feature extraction from plasma experiments for real time control,” funded by ENEA-EURATOM, 2004.

- <sup>1</sup>A. Murari *et al.* Plasma Phys. Controlled Fusion **47**, 395 (2005).
- <sup>2</sup>R. Felton, E. Joffrin, A. Murari, and JET EFDA Contributors, SOFT 2004 Conference, Fusion Eng. Technol. (to be published).
- <sup>3</sup>F. Sartori, A. Cenedese, and F. Milani, Fusion Eng. Des. **66-68**, 735 (2003).
- <sup>4</sup>L. O. Chua and L. Yang, IEEE Trans. Circuits Syst., I: Fundam. Theory Appl. **35**, 1257 (1988).
- <sup>5</sup>Dynamic Image Computing Using Tera-speed Analog Visual Processor (DICTAM) project, <http://www.imse.cnm.es/~dictam>
- <sup>6</sup>L. O. Chua and T. Roska, IEEE Trans. Circuits Syst., I: Fundam. Theory Appl. **40**, 147 (1993).
- <sup>7</sup>S. Espejo, R. Carmona, R. Domínguez-Castro, and A. Rodríguez-Vázquez, Int. J. Circuit Theory Appl. **24**, 341 (1996).
- <sup>8</sup>P. Arena, A. Basile, M. Bucolo, and L. Fortuna, IEEE Trans. Circuits Syst., I: Fundam. Theory Appl. **50**, 837 (2003).
- <sup>9</sup>P. Arena, A. Basile, L. Fortuna, J. Vandewalle, and M. E. Yalcin, Int. J. Circuit Theory Appl. **32**, 519 (2004).
- <sup>10</sup>T. Roska, L. Kek, L. Nemes, A. Zarándy, and P. Szolgay, *CNN Software Library (Template and Algorithms) Version 7.3*, Hungarian Academy of Sciences, Budapest (Hungary: Computer and Automation Institute, 1999).
- <sup>11</sup>A. Rodríguez-Vázquez, G. Linan-Cembrano, L. Carranza, E. Roca-Moreno, R. Carmona-Galan, F. Jimenez-Garrido, R. Domínguez-Castro, and S. Espejo Meana, IEEE Trans. Circuits Syst., I: Fundam. Theory Appl. **51**, 851 (2004).
- <sup>12</sup>A. Zarándy, T. Roska, P. Szolgay, S. Zöld, P. Földesy, and I. Petràs, *European Conference on Circuit Theory and Design-ECCTD'99*, Design Automation Day Proceedings (ECCTD'99-DAD), Stresa, Italy (1999), pp. 69–81.
- <sup>13</sup>P. Arena, A. Basile, R. De Angelis, L. Fortuna, G. Mazzitelli, S. Migliori, G. Vagliasindi, and M. Zammataro, IEEE Trans. Plasma Sci. **33**, 1 (2005).